

Control of Uniaxial Negative Thermal Expansion in Layered Perovskites by Tuning Layer Thickness

Chris Ablitt¹, Arash A. Mostofi^{1,2}, Nicholas C. Bristowe³, and Mark S. Senn^{4,*}

¹ Department of Materials, Imperial College London, London, U.K.

² Department of Physics, Imperial College London, London, U.K.

³ School of Physical Sciences, University of Kent, Canterbury, U.K.

⁴ Department of Chemistry, University of Warwick, Coventry, U.K.

Correspondence*:

Mark S. Senn, Department of Chemistry, University of Warwick, Gibbet Hill, Coventry, CV4 7AL, U.K.

m.senn@warwick.ac.uk

2 ABSTRACT

Uniaxial negative thermal expansion (NTE) is known to occur in low n members of the $A_{n+1}B_nO_{3n+1}$ Ruddlesden–Popper layered perovskite series with a frozen rotation of BO_6 octahedra about the layering axis. Previous work has shown that this NTE arises due to the combined effects of a close proximity to a transition to a competing phase, so called “symmetry trapping”, and highly anisotropic elastic compliance specific to the symmetry of the NTE phase. We extend this analysis to the broader Ruddlesden–Popper family ($n = 1, 2, 3, 4, \dots, \infty$), demonstrating that by changing the fraction of layer interface in the structure (i.e. the value of $1/n$) one may control the anisotropic compliance that is necessary for the pronounced uniaxial NTE observed in these systems. More detailed analysis of how the components of the compliance matrix develop with $1/n$ allows us to identify different regimes, linking enhancements in compliance between these regimes to the crystallographic degrees of freedom in the structure. We further discuss how the perovskite layer thickness affects the frequencies of soft zone boundary modes with large negative Grüneisen parameters, associated with the aforementioned phase transition, that constitute the thermodynamic driving force for NTE. This new insight complements our previous work – showing that chemical control may be used to switch from positive to negative thermal expansion in these systems – since it makes the layer thickness, n , an additional well-understood design parameter that may be used to engineer layered perovskites with tuneable thermal expansion. In these respects, we predict that, with appropriate chemical substitution, the $n = 1$ phase will be the system in which the most pronounced NTE could be achieved.

22 **Keywords:** NTE, perovskite, Ruddlesden-Popper, anisotropy, compliance, corkscrew

1 INTRODUCTION

Ruddlesden–Popper (RP) oxides are an intriguing class of ceramic materials. They have the basic formula $A_{n+1}B_nO_{3n+1}$ and consist of a perovskite block of n corner sharing BO_6 octahedra separated by an AO rock salt layer. Blocks of octahedra are stacked perpendicular to the long crystallographic axis making this layering axis structurally distinct from the two in-plane axes. Neighbouring blocks are de-phased from each other by a lattice translation of $(0.5, 0.5, 0.5)$, and the aristotypical symmetry for any value

28 of n is $I4/mmm$ (Figure 1). As with the perovskites, the A-site chemistry is dominated by larger alkali,
 29 alkali-earth and rare earth metals, and the B-site by transition metals. In the limit $n = \infty$, the perovskite
 30 structure is recovered. While in practice most chemistries are found to predominantly exhibit the $n = 1, 2$
 31 phases only (Palgrave et al. (2012)), in principle any value of n between 1 and ∞ is possible; $n = 3$
 32 structures have been synthesised by careful compositional control (Battle et al. (1998)) and although
 33 $n > 3$ phases are often predicted to be unstable to decomposition (McCoy et al. (1997)), epitaxial growth
 34 techniques have allowed the synthesis of $n = 2 - 5$ (Haeni et al. (2001)), $n = 6$ (Yan et al. (2011)) and
 35 $n = 10$ (Lee et al. (2013)) structures.

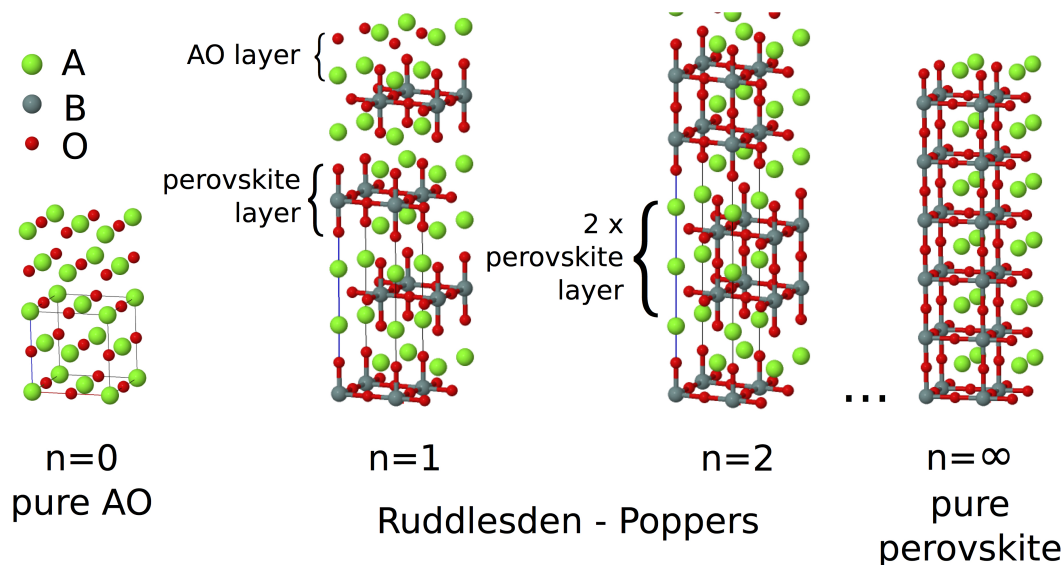


Figure 1. In the $A_{n+1}B_nO_{3n+1}$ Ruddlesden–Popper series, blocks consisting of n layers of ABO_3 perovskite structure are separated by a single layer of AO rock salt structure, with BO_6 octahedra in the next block displaced by a $(0.5, 0.5, 0.5)$ lattice translation. In the $n = \infty$ limit the pure ABO_3 perovskite structure is recovered.

36 One of the most explored systems is the $n = 1$ A_2CuO_4 on account of its high-temperature
 37 superconductivity, where doping of divalent A = Ba and Sr with trivalent rare earth cations has been
 38 extensively investigated (Dwivedi and Cormack (1991)). Superconductivity in these systems is not limited
 39 to the cuprates, and there has been substantial interest in Sr_2RuO_4 (Mackenzie and Maeno (2003)) on
 40 account of its superconducting phase transition below 0.8 K, and in $Sr_3Ru_2O_7$ for its nematic orbitally-
 41 ordered phase (Borzi et al. (2007)). The doped nickelates have also been much studied due to their believed
 42 proximity to a superconducting phase transition, and their charge ordering physics (Yoshizawa et al.
 43 (2000)). More recently, the $n = 2$ member of the RP family has received much attention on the account of
 44 a new form of improper ferroelectricity predicated in $Ca_3Mn_2O_7$ and $Ca_3Ti_2O_7$, termed hybrid improper
 45 ferroelectricity (Benedek and Fennie (2011)). This mechanism circumvents the so-called d^0 criterion for
 46 ferroelectricity, as it does not require an off-centring of cations to drive the phase transition. Instead, this
 47 off-centring (P) may occur as a slave process driven by an octahedral tilt (R_1) and rotation mode (R_2)
 48 of the parent structure that are inherently unstable in some of these systems. This leads to a so-called
 49 trilinear term $\beta R_1 R_2 P$ in the free energy expansion about the parent structure (Benedek et al. (2015))
 50 which, regardless of the sign of the coefficient β , as R_1 and R_2 are inherently unstable, leads to a non-zero
 51 value of the polarisation P (either positive or negative depending on the sign of β).

52 Our contribution to this field of hybrid improper ferroelectricity was to provide experimental confirmation
53 of this mechanism for the case of $\text{Ca}_3\text{Ti}_2\text{O}_7$ (Senn et al. (2015)). However, our high-resolution powder
54 diffraction data for $\text{Ca}_3\text{Mn}_2\text{O}_7$ revealed an added complexity. What was believed to be a single phase
55 at room temperature, having the polar symmetry $A2_1am$, was in fact a mixture of this and a phase that
56 we identified as having $Acaa$ symmetry. Crucially, this phase only has a single octahedral rotation that is
57 out-of-phase rather than in-phase, and the octahedra remain untilted along the c -axis. No hybrid improper
58 ferroelectric mechanism is therefore possible. However, over the large phase coexistence region, which
59 spans a temperature range of 120 K, we did observe pronounced uniaxial negative thermal expansion
60 (NTE) along the c -axis in the $Acaa$ phase. This had not been observed previously in the $n = 2$ system and,
61 although reported in the literature in an analogous $n = 1$ system (Takahashi and Kamegashira (1993)),
62 its significance had not been noted. We were able to explain this NTE phenomenon as being driven by a
63 leftover degree of freedom, the octahedral tilt in the $Acaa$ phase, which remains dynamic.

64 NTE is a rare property, that when it does occur is known to be caused by a diverse range of mechanisms
65 in different materials. Even within inorganic perovskite-based systems, NTE has been found to originate
66 due to coupling of the lattice parameters to: charge ordering (Azuma et al. (2011)), ferroelectric ordering
67 (Chen et al. (2013)) and magnetic and orbital ordering via an invar-like mechanism (Yoshida et al. (2005),
68 Qi et al. (2010)). In framework structures, formed from connected strongly-bonded polyhedral units,
69 NTE has been explained by transverse vibrations of these units, known as rigid-unit modes (RUMs)
70 (Dove et al. (1995), Heine et al. (1999)). We argued in $Acaa$ $\text{Ca}_3\text{Mn}_2\text{O}_7$ that certain vibrational modes
71 with RUM character would have negative Grüneisen parameters and be soft on account of the proximity
72 of the system to the symmetry-forbidden phase transition to $A2_1am$ (Senn et al. (2015)). Using this idea
73 of “trapping” a soft mode in the $Acaa$ phase of $\text{Ca}_3\text{Mn}_2\text{O}_7$ to systematically control and tune the uniaxial
74 thermal expansion properties of the solid solution $\text{Ca}_{3-x}\text{Sr}_x\text{Mn}_2\text{O}_7$ (Senn et al. (2016)), we were able
75 to demonstrate that this is a property exclusively of the $Acaa$ phase in these materials, and that NTE is
76 enhanced as the system approaches the $A2_1am$ phase boundary as a function of chemical composition x .
77 Although other effects operate in related materials, in this study we restrict our discussion to NTE driven
78 by the coupling of the cell parameters to soft lattice modes since it is the most appropriate mechanism to
79 describe our system.

80 The presence of dynamic octahedral tilts in this $\text{Ca}_{3-x}\text{Sr}_x\text{Mn}_2\text{O}_7$ system explained the thermodynamic
81 driving force for NTE along the layering axis. However, the question remained open of why NTE was only
82 observed in this $Acaa$ phase with a frozen in-plane rotation and not in the high-symmetry $I4/mmm$ phase
83 or related ABO_3 perovskite phases, where dynamic octahedral tilts would still operate. We were able to
84 answer this question in a recent computational study using density functional theory (DFT) and working
85 within the quasi-harmonic approximation (QHA) to reproduce experimentally measured uniaxial NTE in
86 the $I4_1/acd$ phase of $n = 1$ Ca_2MnO_4 (Ablitt et al. (2017)).

87 Equation 1 (Grüneisen and Goens (1924)) describes the thermal expansion, $\alpha_\eta(T)$, at temperature, T ,
88 of the three cell axes of a tetragonal crystal ($\eta = 1, 2, 3$ where $\alpha_1 = \alpha_2$ by symmetry). Equation 1 is
89 explained in detail in Appendix 1 and the concept of a Φ vector driving bulk PTE being transformed by
90 a highly anisotropic s into uniaxial NTE (Barron and Munn (1967)) is depicted pictorially in Figure 2.
91 In this picture, the anisotropic thermal expansion is separated into a thermodynamic driving force vector,
92 Φ – arising from the lattice dynamics – that is transformed by the anisotropic elastic compliance matrix,
93 s . By computing the compliance matrix for our NTE phase, we were able to extract the thermodynamic
94 driving force vector from our QHA simulation and found that the effect from dynamic tilts alone would not
95 predict NTE over the wide temperature range observed in experiment. It is only when this thermodynamic

96 driving force is transformed by the highly anisotropic elastic compliance of the layered RP phase that
97 our simulations demonstrated uniaxial NTE of a magnitude and over a temperature range comparable to
98 experiment. Comparing the compliance matrices computed for different phases, we found that particularly
99 high anisotropic compliance is unique to the NTE phase of the RP structure and we linked this anisotropy
100 to combined in-plane (frozen rotations) and out-of-plane (the AO layer) symmetry breaking in the NTE
101 phase.

$$\begin{pmatrix} \alpha_1(T) \\ \alpha_1(T) \\ \alpha_3(T) \end{pmatrix} = \begin{pmatrix} s_{11} & s_{12} & s_{13} \\ s_{12} & s_{22} & s_{13} \\ s_{13} & s_{13} & s_{33} \end{pmatrix} \begin{pmatrix} \Phi_1(T) \\ \Phi_1(T) \\ \Phi_3(T) \end{pmatrix} \quad (1)$$

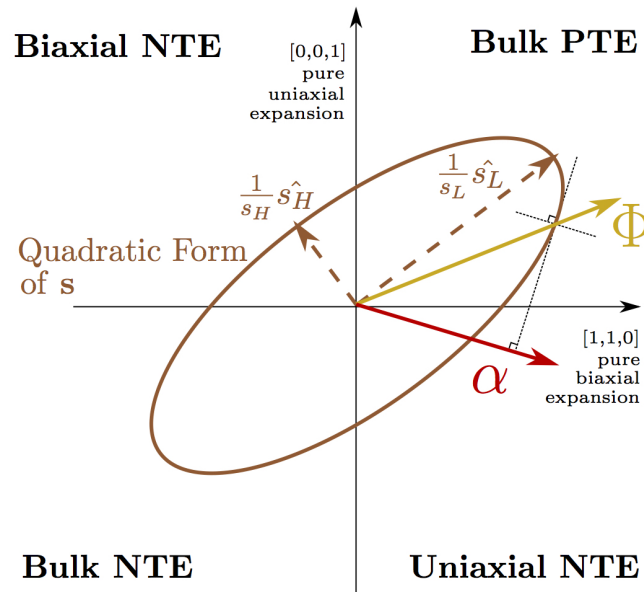


Figure 2. Equation 1 is illustrated on axes describing normal cell deformations using Voigt notation (e.g. where the vector $[\epsilon, \epsilon, 0]$ corresponds to normal strains of ϵ of the a and b axes with the c axis unstrained). A 3×3 elastic compliance matrix s is shown here in its quadratic form as an ellipsoid projected onto the $(\bar{1}, 1, 0)$ plane. s may transform a vector describing the thermodynamic driving force for thermal expansion, Φ , in the positive quadrant (corresponding to bulk positive thermal expansion), into a thermal expansion vector, α , in the quadrant corresponding to uniaxial negative thermal expansion of the c axis. The direction of α is given in the figure by utilising the radius normal property of the representation ellipsoid of the matrix s .

102 Until now, our research has focused on understanding uniaxial NTE in the low n Ruddlesden–Popper
 103 compounds. In the present paper, we focus on extending these concepts to predict how the material
 104 properties that we have linked to NTE develop as a function of n . Studying the $\text{Ca}_{n+1}\text{Ge}_n\text{O}_{3n+1}$ system
 105 within the framework of DFT, we find that the magnitude of anisotropic elastic compliance is dependent
 106 upon the proportion of $\text{CaGeO}_3:\text{CaO}$ interface in the structure – which may be conveniently expressed
 107 by the fraction $1/n$. This high compliance is then maximised with the highest proportion of interface
 108 ($n = 1$). To provide an explanation for this key result, we analyse how the components of the compliance
 109 matrix vary with $1/n$. We identify a series of regimes in which groups of structures display similar elastic
 110 behaviour based on the atomic degrees of freedom allowed by symmetry, and propose mechanisms by
 111 which these internal degrees of freedom couple to cell strains. The most important of these is the atomic
 112 “corkscrew” mechanism that operates at this interface in the NTE phase. We go on to investigate how the
 113 frequencies of the softest (lowest frequency) octahedral tilt modes, which provide the thermodynamic
 114 driving force for NTE, vary as a function of n in the high-symmetry and NTE phases. We find that a higher
 115 proportion of interface causes these phonons to stiffen (increase in frequency) and we infer that within
 116 a given chemical composition, the layer thickness n provides a structural constraint on an approximate
 117 temperature window for which the NTE phase will be stable – where increasing n drives this window to
 118 higher temperatures. One may thus use this insight, combined with our previous discovery that chemical
 119 substitution within a given structure may be used to tune the thermodynamic driving force for NTE, to
 120 use layer thickness n and composition as design parameters to engineer Ruddlesden–Popper phases with
 121 optimal thermal expansion properties.

122 The layout of the paper is as follows: Section 2 gives details of simulation parameters used in this work;
 123 Section 3 (*Results and Discussion*) is then split into 4 subsections: Section 3.1 presents the key result

124 of the paper, showing how the magnitude of anisotropic compliance, linked with uniaxial NTE, varies
125 with $1/n$; for the more interested reader, Sections 3.2 and 3.3 then take a step back and analyse the origin
126 of the result in Section 3.1 in more detail, in Section 3.2 by analysing how the different elements of the
127 compliance matrix evolve with $1/n$ and in Section 3.3 by identifying different compliance regimes linked to
128 crystallographic degrees of freedom in the structure that couple to strain; finally in Section 3.4 we consider
129 how the thermodynamic driving force for NTE varies with $1/n$ by presenting lattice dynamics calculations
130 investigating phonons corresponding to tilts of GeO_6 octahedra in $\text{Ca}_{n+1}\text{Ge}_n\text{O}_{3n+1}$, and compare these
131 results against experimental phase diagrams constructed with data taken from the literature of the analogous
132 $\text{Ca}_{n+1}\text{Mn}_n\text{O}_{3n+1}$ system. Additionally, Appendix 1 gives a brief overview of the mathematical concepts
133 relevant for the study of thermal expansion in an anisotropic material and Appendix 2 outlines the symmetry
134 of the phases simulated throughout this study.

2 METHODS

135 Calculations were performed using CASTEP, a plane-wave density functional theory (DFT) code, version
136 7.0.3 (Clark et al. (2005)). A plane wave cut-off energy of 1400 eV was employed for all calculations with
137 electron density stored on a grid twice as dense. A $7 \times 7 \times 2$ Monkhorst–Pack grid of kpoints shifted away
138 from the Γ -point was used for calculations of the 14 atom $I4/mmm$ phase of ($n = 1$) Ca_2GeO_4 , with grids
139 of equivalent reciprocal space density used for all other structures (high-symmetry and rotation phases
140 for $n = 1, 2, 3, 4, \infty$ - see Appendix 2). Norm-conserving pseudopotentials, generated on-the-fly using
141 CASTEP version 16.0, were used for all calculations and the associated pseudopotential strings may be
142 found Table S1 in the SI. All calculations used the PBEsol exchange-correlation functional (Perdew et al.
143 (2008)). Absolute energies were converged to an accuracy of 0.5 meV/atom with respect to k-point grid
144 density and plane wave cut-off energy. Geometric relaxations were performed with a force tolerance of
145 10^{-4} eV/Å and a stress tolerance of 10 MPa.

146 We expect our $\text{Ca}_{n+1}\text{Ge}_n\text{O}_{3n+1}$ system to be well-described by conventional GGA density functionals.
147 There are other members of the chemical space that might require more careful consideration in terms of
148 the appropriate methodology, such as hybrid functionals, DFT+U, or potentially even DMFT in order to
149 accurately describe the physics associated with localised d and f-electrons.

150 Elastic constants were computed by fitting 2nd order polynomials to the energies of cells with applied
151 strains of +/- 0.2, 0.4% from the fully relaxed cell, where the internal degrees of freedom (the atomic
152 positions) were free to relax. The quadratic terms to these fits were used to construct terms within the elastic
153 constant matrix, c , and this matrix inverted to compute the elastic compliance matrix, s (see Appendix 1
154 for the definition of s studied).

155 Bulk moduli, K , were computed by allowing the cell and all internal degrees of freedom to relax in
156 response to hydrostatic pressures in the range -2 to +2 GPa. The bulk modulus was then found by fitting
157 the computed relaxed volume, V , as a function of the external pressure, P , to the equation: $K = -\frac{d(\ln[V])}{dP}$.
158 The bulk compressibility, β , is then given by $\beta = K^{-1}$.

159 Density functional perturbation theory (DFPT) was used within CASTEP (Refson et al. (2006)) to
160 perform phonon calculations. In the present study, only phonon frequencies computed at single, high
161 symmetry q-points are reported. In $n = 1, 3, \infty$ phases, these are at the X ($1/2, 1/2, 0$) and P ($1/2, 1/2, 1/2$)
162 points in the $I4/mmm$ high-symmetry phase (labelled M and R respectively in $n = \infty Pm\bar{3}m \text{ABO}_3$) and
163 for $n = 2, 4$ phases at the X -point in $I4/mmm$. Phonons in child rotation phases were always computed at
164 the Γ -point. In every compound studied, the initial structure was the highest symmetry phase that was fully

165 relaxed. All child phases were found by freezing unstable phonons (modes with imaginary frequencies)
 166 into the structure with small amplitudes and allowing this child structure to relax. The lattice parameters
 167 and cell energies relative to the high-symmetry parent of all relaxed structures may be found in Table S2 in
 168 the SI.

3 RESULTS AND DISCUSSION

169 3.1 Anisotropy of the Compliance Matrix

170 It was previously shown in first-principles calculations performed on the NTE phase of Ca_2GeO_4 (i.e. the
 171 $I4_1/acd$ rotation phase) that a highly anisotropic s is an essential ingredient for uniaxial NTE in this system
 172 (Ablitt et al. (2017)). κ , as defined in Equation 2, is the ratio of the highest (s_H) and lowest (s_L) eigenvalues
 173 of s and gives a measure of the anisotropy of s ; where higher κ indicates that s is more conducive to
 174 uniaxial NTE. Figure 3 therefore shows how s_H , s_L and κ evolve with varying n for high-symmetry and
 175 rotation phases in the $\text{Ca}_{n+1}\text{Ge}_n\text{O}_{3n+1}$ series.

$$\kappa = \frac{s_H}{s_L} \quad (2)$$

176 In the composite mechanics community, the elastic properties of laminates are typically described by
 177 the properties of the constituent phases, weighted by the relative fraction of that phase (Sarlosi and Bocko
 178 (2016)). However, in the functional oxides community, it is well known that the local structure of atomic
 179 interfaces within a crystal often dictate the physical properties of the entire material (Int (2012)). There
 180 are therefore two ways to conceive the layered Ruddlesden–Popper structure shown in Figure 1: (i) as
 181 being comprised of constituent CaGeO_3 and CaO phases or (ii) as being comprised of CaGeO_3 and the
 182 $\text{CaGeO}_3:\text{CaO}$ interface.

$$\text{Ca}_{n+1}\text{Ge}_n\text{O}_{3n+1} = [\text{CaGeO}_3]_n [\text{CaO}] = [\text{CaGeO}_3]_{n-1} [\text{CaGeO}_3 : \text{CaO}] \quad (3)$$

183 From Equation 3, it is clear that (i) the mole fraction of CaO in $\text{Ca}_{n+1}\text{Ge}_n\text{O}_{3n+1}$ is given by the ratio
 184 $1/(n + 1)$ and (ii) the mole fraction of Ca_2GeO_4 , which represents the fraction of $\text{CaGeO}_3:\text{CaO}$ interface
 185 in the structure, is given by the ratio $1/n$. Therefore to reflect the importance of the interface, s_H , s_L
 186 and κ are plotted as a function of $1/n$ in the subplots on Figure 3. Straight lines have also been plotted
 187 interpolating between values for the CaGeO_3 ($1/n = 0$) and Ca_2GeO_4 ($1/n = 1$) end members to show
 188 how well the structure may be considered as a mixture of these two constituents in the high-symmetry
 189 (blue dot-dashed) and rotation (red dotted) phase series.

190 The least compliant eigenvector, s_L , corresponds to isotropic expansion/contraction for all structures
 191 investigated (see Table S3 in SI) and thus is closely linked to the bulk compressibility, β . Figure 3 shows
 192 that s_L increases linearly with higher Ca_2GeO_4 mole fraction but is invariant to changes in symmetry for a
 193 given n . All values for s_L lie on the line interpolating between CaGeO_3 and Ca_2GeO_4 high-symmetry end
 194 members regardless of phase symmetry implying that s_L is determined mainly by the composition.

195 s_H also increases in magnitude with Ca_2GeO_4 content for all RP phases. However, unlike s_L , s_H is
 196 greatly enhanced in the phase with a frozen rotation compared to the high-symmetry phase, and the rate of
 197 increase in s_H for rotation phases with $1/n$ is also greater in the rotation phase than in the high-symmetry
 198 parent. For all the tetragonal phases studied, the eigenvector s_H lies in a strain direction corresponding

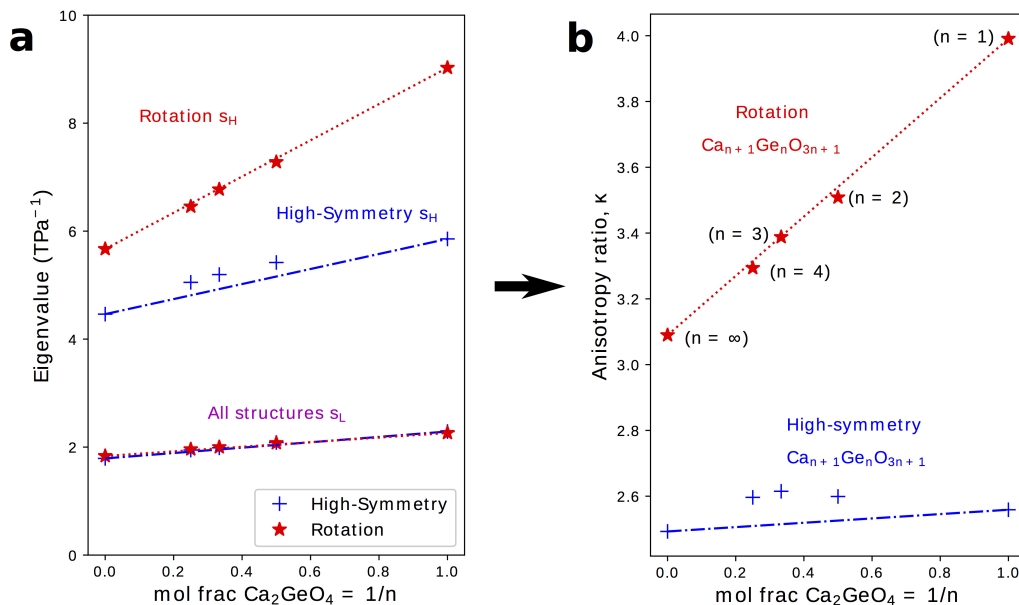


Figure 3. **a** Lowest, s_L and highest, s_H , eigenvalues to the compliance matrix, \mathbf{s} , and **b** the anisotropy ratio κ plotted for high-symmetry and rotation phases in the $\text{Ca}_{1+n}\text{Ge}_n\text{O}_{3n+1}$ series against the mole fraction of $\text{CaGeO}_3:\text{CaO}$ interface ($1/n$). Interpolations between values in the CaGeO_3 ($1/n = 0$) and Ca_2GeO_4 ($1/n = 1$) structures are plotted for both high-symmetry and rotation phases (blue dot-dashed and red dotted lines respectively).

199 to a cooperative increase in in-plane lattice parameters, ab , and decrease in the lattice parameter along
 200 the layering axis, c , or visa versa. In a previous work, we proposed an atomic mechanism to facilitate a
 201 large compliance eigenvector in Ruddlesden–Popper phases with a frozen octahedral rotation that relies
 202 on combined in-plane and out-of-plane symmetry breaking at the $\text{CaGeO}_3:\text{CaO}$ layer interface to closely
 203 couple the ab and c axes (Ablitt et al. (2017)). Since this mechanism operates at the $\text{CaGeO}_3:\text{CaO}$ interface,
 204 it is interesting to note that s_H in the rotation phase is linearly dependent upon the mole fraction of this
 205 interface in the structure, increasing as this interface fraction becomes greater, and thus s_H for intermediate
 206 values of $1/n$ may be easily predicted by interpolating between the s_H values for CaGeO_3 (with no
 207 interface) and Ca_2GeO_4 (maximum interface) rotation phases.

208 This steeper increase in s_H for rotation phases than high-symmetry phases with interface mole fraction
 209 ($1/n$) thus manifests as a large enhancement in κ between the child structure and parent, where the
 210 magnitude of this enhancement increases greatly with $1/n$, reaching a maximum in the $n = 1$ structure.
 211 The key result of this analysis of the compliances is hence that this $n = 1$ structure is the best in the
 212 Ruddlesden–Popper series for facilitating uniaxial NTE.

213 3.2 Elastic Compliances

214 Figure 3 showed how the eigenvalues of \mathbf{s} vary with the $\text{CaGeO}_3:\text{CaO}$ interface fraction ($1/n$). In this
 215 section we take a step back and analyse how the individual components of the compliance matrix, s_{ij} , vary
 216 with $1/n$. In the second half of the section, we assess the quality of the two interpolations, (i) between
 217 CaGeO_3 and CaO constituents and (ii) between CaGeO_3 and $\text{CaGeO}_3:\text{CaO}$ interface constituents, to predict
 218 the compliance components of intermediate values of $1/n$.

219 Figure 4 shows the elastic compressibility, β , and components of the elastic compliance matrix, s ,
 220 computed for fully relaxed high-symmetry and rotation phases in the $\text{Ca}_{n+1}\text{Ge}_n\text{O}_{3n+1}$ series. Since all
 221 phases are (pseudo-)tetragonal, only the 4 symmetrically distinct s_{ij} components identified in Equation 1
 222 are plotted. The full s matrix, associated eigenvalues and eigenvectors and β may be found for all structures
 223 in Table S3 in the SI.

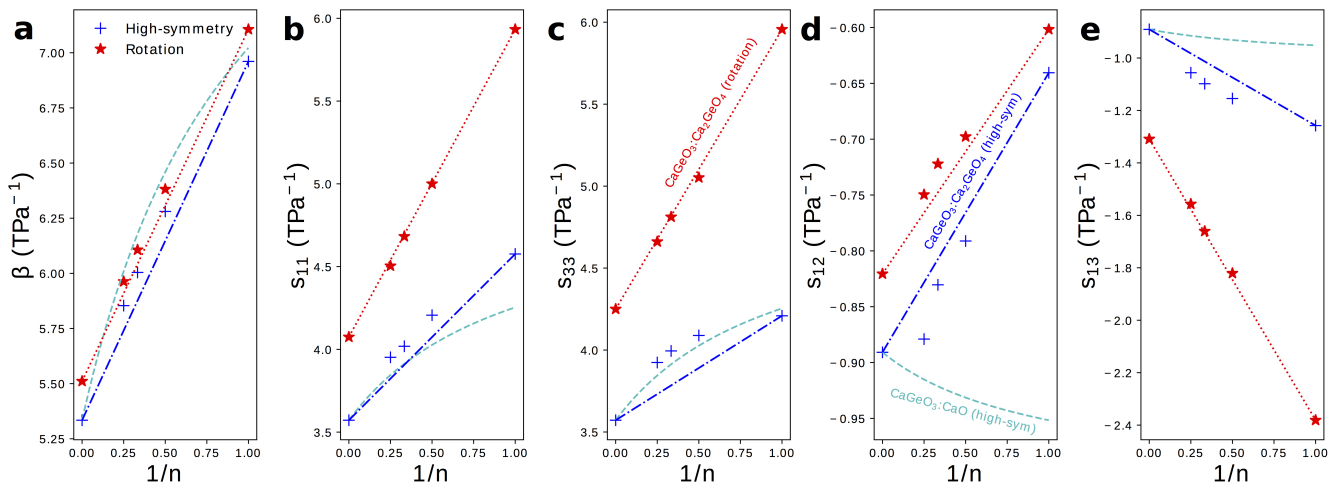


Figure 4. **a** The bulk compressibility, β and **b-e** components s_{ij} of the elastic compliance matrix for a tetragonal material plotted for high-symmetry and rotation phases in the $\text{Ca}_{1+n}\text{Ge}_n\text{O}_{3n+1}$ series against the mole fraction of $\text{CaGeO}_3:\text{CaO}$ interface ($1/n$). Interpolations between values in the CaGeO_3 ($1/n = 0$) and Ca_2GeO_4 ($1/n = 1$) structures are plotted for both high-symmetry and rotation phases (blue dot-dashed and red dotted lines respectively). A third curve shows the interpolation between values in the $Pm\bar{3}m$ CaGeO_3 phase and CaO rock salt structure computed as a function of CaO mole fraction $1/(n+1)$ (cyan dashed).

224 The bulk elastic compressibility, β , increases linearly with $1/n$ but only very slight enhancement in
 225 compressibility is seen between the high-symmetry and rotation phases for a given n . Differences in β
 226 can therefore not be used to explain why uniaxial NTE is common in low n RP rotation phases but not in
 227 parent $I4/mmm$ phases.

228 The normal compliance components, s_{11} and s_{33} , also increase with $1/n$ but unlike in β there is a
 229 significant enhancement in the rotation phase compared to the high-symmetry parent, with both the
 230 magnitude and gradient with respect to $1/n$ greater in the rotation phase.

231 The sign of the off-diagonal compliance components, s_{12} and s_{13} , that couple normal stresses to normal
 232 strains between axes, are negative for all compounds. This indicates that all materials have all positive
 233 Poisson ratios, ν_{ij} , where ν_{ij} describes the normal strain of axis j in response to a strain of axis i
 234 ($\nu_{ij} = -\frac{\epsilon_j}{\epsilon_i}$). Most materials have $\nu_{ij} > 0$, so these NTE RP phases are not auxetic ($\nu_{ij} < 0$), even though
 235 auxetic materials have been linked with materials that exhibit anisotropic NTE (Wang et al. (2017)).

236 Despite the negative sign, the behaviour of s_{13} is similar to that of s_{11} and s_{33} : compliance increases with
 237 $1/n$ and there is a large enhancement in both the magnitude and the gradient increase with $1/n$ in the NTE
 238 phase compared with the high-symmetry parent. s_{12} , on the other hand, displays the opposite trend since
 239 the magnitude of coupling decreases with $1/n$ and going from the high-symmetry to rotation phases.

240 As in Figure 3, straight lines have been plotted on the subplots in Figure 4 interpolating between values
241 for the CaGeO_3 ($1/n = 0$) and Ca_2GeO_4 ($1/n = 1$) end members. A third dashed cyan line has been added
242 to interpolate between the pure high-symmetry CaGeO_3 and CaO rock salt constituent phases. Because
243 the mole fraction of CaO is actually expressed as $1/(n + 1)$ (Equation 3) these lines appear curved when
244 plotted against the $1/n$ x-axis.

245 The trend in β follows that that would be predicted by modelling the Ruddlesden–Popper series as
246 a laminate of CaGeO_3 and CaO, suggesting that β is determined predominantly by the composition.
247 Since bulk volume thermal expansion, α , is proportional to the bulk compressibility, β , this implies
248 that the magnitude of α is heavily dependent on chemistry. This result echoes recent work showing that
249 experimental measurements of many thermodynamic properties of Ruddlesden–Popper structures may be
250 predicted by interpolating between values of their chemical constituents (Glasser (2017)).

251 Whereas β could be approximated well as a function of CaO content for RP phases, s_{11} of high-symmetry
252 phases increases above that predicted by the cyan curve. This indicates that even in the high-symmetry
253 phase, the CaGeO_3 and CaO layers do not behave independently and are affected by the interface between
254 them. The prediction for s_{33} based on the CaO content is quite good, which may be because s_{33} corresponds
255 to deformations along the layering axis (with 0 strain boundary conditions on the a and b axes) and therefore
256 the different constituent layers are being squashed in series¹. For both s_{11} and s_{33} , the rotation phases
257 follow a linear relationship with $1/n$ and therefore may be considered dependent upon the fraction of
258 CaGeO_3 :CaO interface in the structure (red dotted line). However, in the high-symmetry phase the $n > 1$
259 values for both normal compliance components increase slightly beyond that predicted by interpolating
260 between the extreme CaGeO_3 and Ca_2GeO_4 values (blue dot-dashed line). This is surprising since it is not
261 immediately obvious how the structure of higher n compounds is different to local regions of CaGeO_3 and
262 Ca_2GeO_4 and therefore what additional compliance mechanisms could operate.

263 For both s_{12} and s_{13} , modelling the compliance according to the mole fraction of CaO is a poor
264 approximation, so much so that this prediction actually gives the wrong sign of the change in s_{12} with $1/n$.

265 3.3 Compliance Enhancement Mechanisms

266 In Section 3.2 we showed that certain elastic properties, such as the bulk compressibility, β , are insensitive
267 to small changes in crystal symmetry and may be accurately predicted by interpolating between the value
268 of β in CaGeO_3 and CaO end member structures based on the mole fraction of CaO. However, components
269 of the anisotropic compliance matrix, s_{ij} , typically differ in magnitude between high and low symmetry
270 phases and are generally more compliant than a CaGeO_3 :CaO interpolation predicts. Figure 5 shows the
271 same plot as in Figure 4.e (s_{13} vs $1/n$) but with annotations decomposing the s_{13} behaviour of different
272 structures into regimes of increasingly enhanced compliance. By separating the compliance regimes in this
273 way, in this section we discuss the atomic displacements allowed in each regime by the phase symmetry and
274 thus propose atomic mechanisms that may explain these enhancements in the s_{13} axis coupling parameter.
275 In many cases (although not discussed here) this analysis may be used to explain the different regimes of
276 the s_{11} , s_{33} and s_{12} components in Figure 4.

277 Taking the value of s_{13} that would be predicted by interpolating between values in the CaGeO_3 and CaO
278 constituent structures as a base (the dashed cyan curve in Figure 5), arrow ① represents an increase in
279 the coupling between in-plane (a and b) axes and the layering axis (c) in the $n = 1$ Ca_2GeO_4 $I4/mmm$

¹ However, we note that under these conditions one should use a Voigt average to interpolate s_{33} , whereas by drawing a straight line of compliance vs mole fraction we have actually performed a Reuss interpolation. In the Figure S1 in the SI we show that a Voigt fit against CaO mole fraction is actually less close.

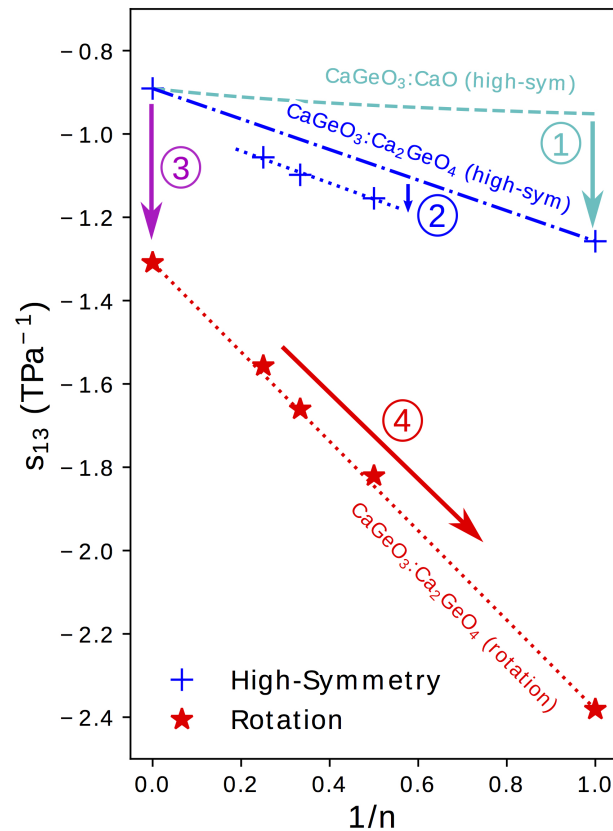


Figure 5. The s_{13} term of the elastic compliance matrix (corresponding to coupling between an in-plane axis, a or b , and the layering axis, c) for a tetragonal material plotted for high-symmetry and rotation phases in the $\text{Ca}_{1+n}\text{Ge}_n\text{O}_{3n+1}$ series against the mole fraction of $\text{CaGeO}_3:\text{CaO}$ interface ($1/n$). Numbered arrows show the enhancement in compliance between different regimes represented by lines.

280 phase. In a pure cubic ABO_3 perovskite, the A cations by symmetry have the same z position as the apical
 281 O anions. However, the inclusion of the AO layer in high-symmetry RP phases causes symmetry breaking
 282 along c at the $\text{ABO}_3:\text{AO}$ interface such that the apical O and interfacial A ions are no longer restricted to
 283 the same z coordinate, leading to a so-called “rumpling” of the AO layer. We propose that this rumpling
 284 facilitates a mechanism for enhanced s_{13} coupling illustrated in Figure 6.a: As the in-plane, ab , axes are
 285 strained, the interstitial void between BO_6 octahedra below the interfacial A cation changes in size, but
 286 the rumpling adds a degree of freedom to the z coordinate of the A cation which may thus move further
 287 into/out of the void in response to the in-plane strain. This thus couples the in-plane, ab , axes to internal
 288 displacements along the layering axis c and therefore to the layering axis itself.

289 It was commented in the preceding section that the enhancement in compliance from the interpolation
 290 between CaGeO_3 and Ca_2GeO_4 values to $n > 1$ high-symmetry RP structures (shown by arrow ②
 291 in Figure 5) is surprising since all structures consist of a $\text{CaGeO}_3:\text{CaO}$ interface (with rumpling of the
 292 CaO z positions) and blocks of CaGeO_3 (that one might expect to behave as bulk cubic CaGeO_3). Close
 293 inspection of the $n = 1$ and $n = 2$ $I4/mmm$ phases in Figure 1 allows us to see that in A_2BO_4 structures,
 294 the length of all apical B–O bonds are equal due to the mirror symmetry plane lying in each BO_6 layer.
 295 Similarly the angle between epitaxial B–O and apical B–O bonds must be 90° by the same reasoning.
 296 However, in $\text{A}_3\text{B}_2\text{O}_7$ $I4/mmm$ phases, this restriction that the perovskite blocks must contain a mirror
 297 plane at the centre only means that the two outer apical B–O bond lengths and BO_6 internal angles must

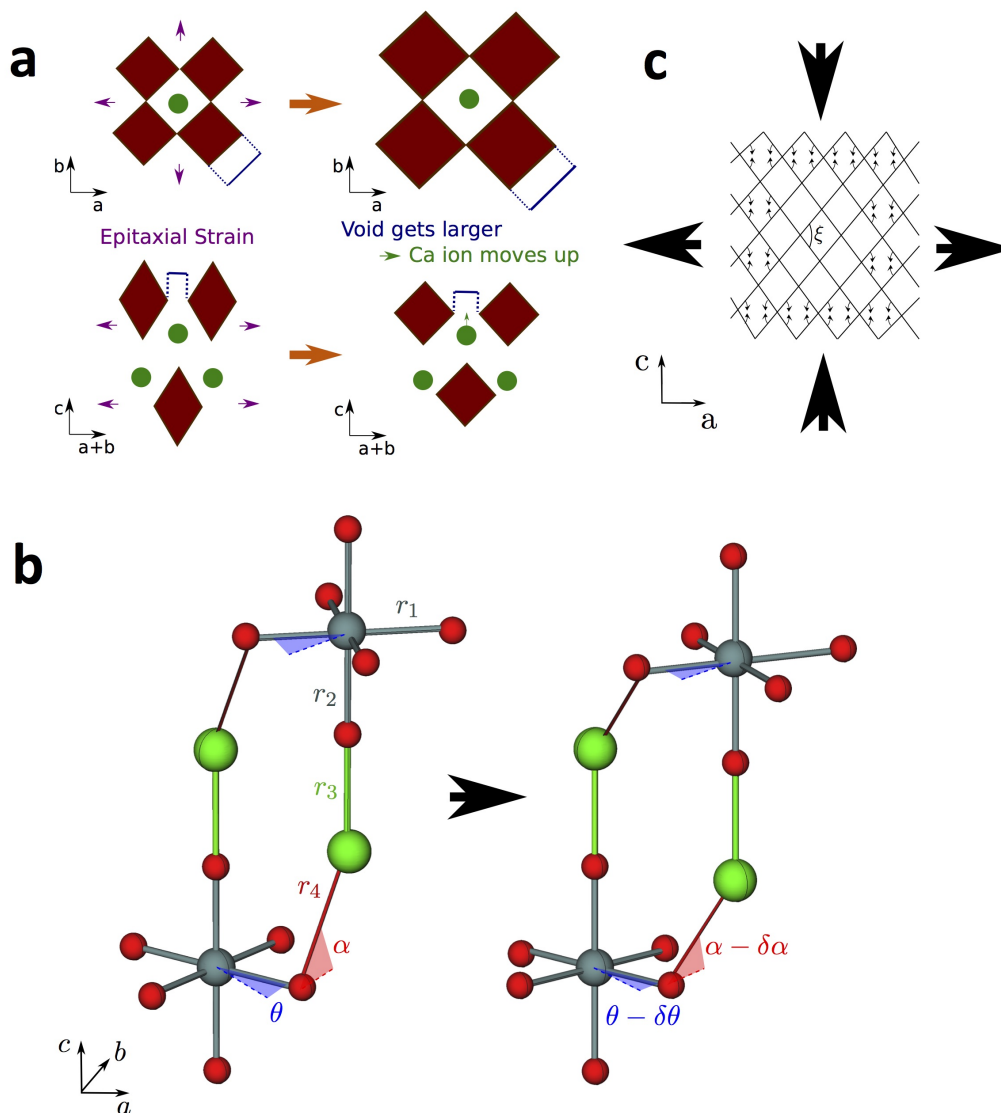


Figure 6. Strain coupling mechanisms that make structures particularly compliant to cooperative strains. Since these mechanisms couple the a (and/or b) and c axes, they are typified by large s_{13} off-diagonal components of the compliance matrix. **a** Mechanism for increased compliance in $I4/mmm$ RP structures where the rumpling between the interfacial A and apical O ions means that A is free to displace independently of O in response to in-plane strains; **b** corkscrew mechanism in RP rotation phases – the structure is able to couple in-plane tensile strains to compressive strains along c via internal displacements assuming all nearest neighbour B–O bonds and the two shortest A–O bonds do not deform (shown as rigid struts labelled r_1 – r_4) by changing the angle of in-plane and out-of-plane hinges (described by the angles θ and α as shown); **c** wine rack structure where tensile strains along a may couple to compressive strains along c in a system of rigid struts in a trellis structure by only changing the angle ξ .

298 be equal and the apical B–O bond lengths between the two inner BO_6 layers must be equal. There is no
 299 restriction by symmetry that all apical B–O bond lengths must be equal or in fact that all BO_6 internal
 300 angles must be 90° . These weaker restrictions create internal degrees of structural freedom that may
 301 facilitate greater compliance, since there is greater freedom for the atoms to move in response to external
 302 strains. In structures relaxed using DFT, we find that there are slight differences in these two bondlengths:
 303 1.87 \AA and 1.90 \AA for the outer and inner apical B–O bonds respectively, and the angle between outer
 304 apical B–O and epitaxial B–O bonds is 91.2° . This same argument may be applied to all $n > 1$ $I4/mmm$

305 phases. However, in the special case of the $n = \infty$ series end member, there is no AO layer to break
 306 any symmetry along c and thus all B–O bond lengths are equal and all O–B–O angles are 90° . That this
 307 difference between s_{13} of $n = 2, 3, 4$ high-symmetry phases and the $\text{CaGeO}_3:\text{Ca}_2\text{GeO}_4$ interpolation is
 308 not also seen in the significantly more compliant rotation phases may be because in these rotation phases,
 309 additional compliance mechanisms operate that dwarf the effect described by arrow (2).

310 Arrow (3) in Figure 5 represents the increase in coupling between the a/b and c axes from the cubic
 311 CaGeO_3 phase to an $I4/mcm$ phase with anti-phase octahedral rotation about the c axis. From a structural
 312 symmetry point of view, this may again come as a surprise since the $I4/mcm$ phase only has an internal
 313 degree of freedom in the ab plane and not along the c axis that this plane couples to. Therefore one might
 314 expect large changes in in-plane strain in response to biaxial stress from rigid BO_6 octahedra rotating,
 315 but not also large changes in c . However, DFT studies on LaAlO_3 (Hatt and Spaldin (2010)) and LaNiO_3
 316 (Weber et al. (2016)) show that while the application of compressive biaxial strain to the $I4/mcm$ causes
 317 the rotation angle to increase, it also leads to a large tetragonal distortion of the BO_6 units with compression
 318 of the epitaxial B–O bonds and extension of the apical B–O bonds.

319 Finally, arrow (4) in Figure 5 represents the increase in s_{13} coupling between rotation phases of CaGeO_3
 320 perovskite and RP phases with a frozen octahedral rotation. In these phases, the rumpling of the interfacial
 321 AO layer identified in the high-symmetry structure is still present. However, whereas in the high-symmetry
 322 structure, in-plane strains necessarily involved deformations of stiff epitaxial B–O bonds, in this lower-
 323 symmetry phase, the frozen in-plane octahedral rotation adds an internal degree of freedom in the in-plane
 324 epitaxial O positions. There are thus internal degrees of freedom in both in-plane and layering axes in
 325 RP rotation phases. In our previous paper (Ablitt et al. (2017)) we proposed a “corkscrew” mechanism
 326 to explain high s_{13} coupling in RP1 rotation phases but not in $I4/mcm$ ABO_3 phases. This coupling
 327 mechanism in theory allows a and c to deform cooperatively without extending the four most stiff cation-
 328 anion bonds identified in the $I4_1/acd$ Ca_2GeO_4 structure, by only changing two bond angles, labelled θ
 329 and α in Figure 6.b. We call this mechanism “corkscrew” since an in-plane rotation leads to an extension
 330 along the rotation axis: Figure 6.b shows how the in-plane rotation angle θ may decrease in response to
 331 a biaxial expansion, such that this in turn pulls the stiff O–A bond (shown as a rigid rod), decreasing the
 332 angle α and thus increasing the rumpling of the rock salt layer and forcing contraction along the c -axis.

333 The net result of these interfacial strain coupling mechanisms in RP phases, yielding an enhanced
 334 off-diagonal s_{13} compliance term, is rather reminiscent of the “wine-rack” mechanism such as that
 335 which operates in methanol monohydrate (Fortes et al. (2011)). In the wine-rack trellis structure, shown
 336 schematically in Figure 6.c with rigid struts but flexible hinges, a couples strongly to c , mediated by the
 337 hinge angle, ξ , in the ac plane. Following the method used to analyse the wine-rack (Grima and Evans
 338 (2000)) and other idealised geometries (Smith et al. (2000), Grima et al. (2012)), we were able to derive the
 339 mechanical properties that our pure “corkscrew” mechanism would exhibit under the conditions that the
 340 four *stiff* bonds shown in Figure 6.b indeed remained rigid and all resistance to strain came from a harmonic
 341 potential in the θ and α -hinges (Ablitt et al. (in preparation)). Under these restrictions, a “corkscrew” model
 342 would have an s_{13} compliance parameter as a function of RP layer thickness, n , given by

$$s_{13} = - \frac{f(\theta, \alpha) r_1^3}{\left[n k_\theta + k_\alpha \left(\frac{d\alpha}{d\theta} \right)^2 \right]}, \quad (4)$$

343 where k_θ and k_α represent the harmonic stiffness of the θ and α -hinges, respectively, and $f(\theta, \alpha)$ is an
 344 expression of trigonometric functions of θ and α

$$f(\theta, \alpha) = \frac{\sin(2\theta) [\sin(\theta) + \cos(\theta)]}{4 \tan(\alpha)}. \quad (5)$$

345 Under the constraints of this model, α is explicitly dependent on θ by the equation

$$r_4 \cos(\alpha) = r_1 [\cos(\theta) - \sin(\theta)], \quad (6)$$

346 and therefore given the bond lengths r_1 - r_4 (as defined in Figure 6.b), the value of θ fully determines the
 347 structure.

348 In the limit that $k_\alpha \gg k_\theta$, the AO interface is stiffer than the ABO_3 perovskite blocks and s_{13} loses
 349 dependence on n . However, in the opposing limit that $k_\theta \gg k_\alpha$ and changing the in-plane rotation angle
 350 is the main obstacle to strain, $s_{13} \propto 1/n$. The real system is closer to the $k_\theta \gg k_\alpha$ limit as we observe
 351 linear behaviour of s_{13} with $1/n$. Although this model has been derived assuming that all epitaxial B–O
 352 bond lengths (r_1) and all apical B–O bond lengths (r_2) are equal, the bond lengths r_2 and r_3 do not feature
 353 in Equation 4 and r_1 and θ only need refer to the in-plane bond lengths and rotation angle in the outer
 354 layer of the perovskite block. Therefore this mechanism is compatible with a distribution of possible bond
 355 lengths and rotation angles in different layers of a perovskite block if $n > 1$.

356 We accept the limitations of such simple models but developing the study of how symmetry-allowed
 357 local distortions can give rise to new compliance mechanisms in different crystallographic phases, such as
 358 those identified using arrows (1)-(4) in Figure 5, may allow for the prediction of phases with high cross
 359 compliances by symmetry alone, before needing to explicitly compute the elastic constants. Calculations of
 360 elastic constants are, in turn, frequently less expensive than performing lattice dynamics calculations across
 361 the full Brillouin zone to compute the thermodynamic driving force for anisotropic thermal expansion, Φ .

362 Therefore, looking for other materials with such high cross compliances, using symmetry analysis as
 363 a guide to narrow the pool of structures, may prove a more general method for searching for novel NTE
 364 materials. Indeed, by considering this analysis and our thermodynamic criteria requiring a proximity to a
 365 competing phase transition to provide Φ , we have already been able to identify (Ablitt et al. (2017)) the
 366 layered double perovskites Sr_2MgWO_6 (Achary et al. (2006)) and (110)-cut perovskite LaTaO_4 (Cordrey
 367 et al. (2015)) which fall within this general paradigm. Substantial research opportunities exist in this area
 368 to more fully explore the NTE behaviour of these classes of materials.

369 3.4 Dynamic Driving Force for NTE

370 So far we have not addressed the thermodynamic driving force for thermal expansion $\Phi(T)$, and it
 371 is rather more computationally expensive to calculate than κ as it requires the full phonon density of
 372 states to be computed for different strained structures within the quasi-harmonic approximation (QHA).
 373 Furthermore, this procedure is only possible if all phonons within the NTE structure simulated using
 374 DFT have real frequencies – suggesting that the phase must be stable at 0 K. For $n > 1$ structures in the
 375 $\text{Ca}_{1+n}\text{Ge}_n\text{O}_{3n+1}$ series, this latter condition is not met, and therefore full computation of $\Phi(T)$ as we
 376 performed previously (Ablitt et al. (2017)) would not be possible. However, we also previously identified
 377 that the most important modes driving NTE are octahedral tilts about an in-plane axis. Thus in Figure 7
 378 we have plotted the frequency of the lowest frequency tilt mode to occur at a high-symmetry q-point in

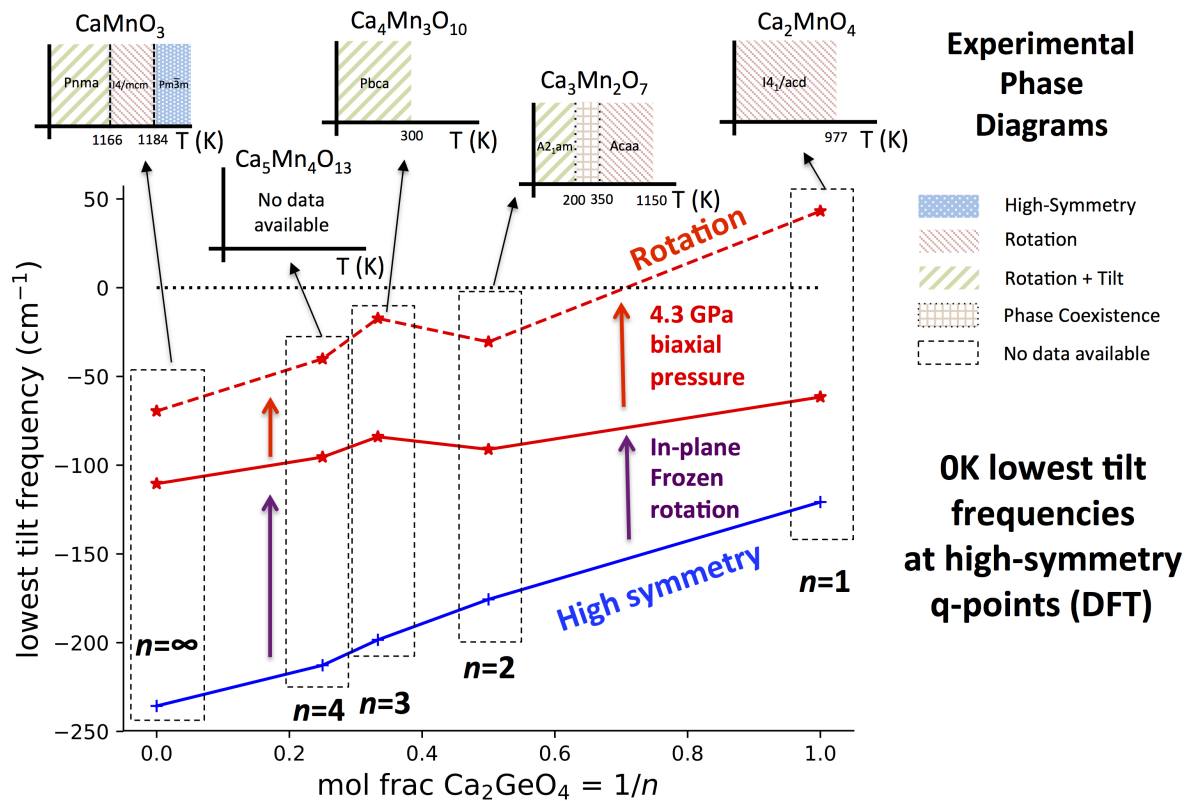


Figure 7. The lowest frequency harmonic phonon mode with octahedral tilt character found in DFT simulations at high-symmetry q -points in the $\text{Ca}_{1+n}\text{Ge}_n\text{O}_{3n+1}$ series against interface fraction, $1/n$. Tilt frequencies have been plotted in the high-symmetry and rotation phases with 0 GPa external pressure, and also for the rotation phase with a 4.3 GPa biaxial pressure applied to give better agreement of the $\text{Ca}_{1+n}\text{Ge}_n\text{O}_{3n+1}$ structure to $\text{Ca}_{1+n}\text{Mn}_n\text{O}_{3n+1}$. DFT only simulates the system at 0 K whereas phonon frequencies may harden with increased temperature. This means that many octahedral tilts are predicted with imaginary frequencies (shown as negative) even if the mode has a real frequency and the structure is stable at some higher temperature. To give an idea of how the equilibrium phase changes with temperature, the inset graphs plot the experimentally observed phase diagram for each n in the $\text{Ca}_{1+n}\text{Mn}_n\text{O}_{3n+1}$ system. The data to make these illustrations was taken from: Ca_2MnO_4 (Takahashi and Kamegashira (1993)); $\text{Ca}_3\text{Mn}_2\text{O}_7$ (Senn et al. (2015)); $\text{Ca}_4\text{Mn}_3\text{O}_{10}$ (Battle et al. (1998)); CaMnO_3 (Taguchi et al. (1989)).

379 high-symmetry phases and phases with a frozen in-plane rotation. We note that these tilts are not the same
 380 as the vibrations of ions along the z direction predicted using a QHA-inspired method to cause NTE in a
 381 $A2_1am$ $\text{Ca}_3\text{Ti}_2\text{O}_7$ phase after 30 GPa hydrostatic pressure has been applied and in which these octahedral
 382 tilts are already frozen (Huang et al. (2016)). As in previous studies (Senn et al. (2016), Ablitt et al. (2017))
 383 the $\text{Ca}_{1+n}\text{Ge}_n\text{O}_{3n+1}$ series is being treated as an analogue to $\text{Ca}_{1+n}\text{Mn}_n\text{O}_{3n+1}$ for comparison against
 384 experimental data to avoid expensive magnetic calculations since Ge^{4+} and Mn^{4+} are known to have equal
 385 ionic radii (Shannon (1976)). The authors have previously shown that this substitution has little bearing on
 386 the properties (phonon frequencies, elastic constants) relevant to modelling thermal expansion within the
 387 quasi-harmonic approximation.

388 It can be seen from Figure 7 that in all phases, the frequency of the softest tilt mode stiffens with increased
 389 Ca_2GeO_4 content, indicating that the inclusion of the $\text{CaGeO}_3:\text{CaO}$ interface reduces the propensity of
 390 octahedra to tilt. The tilt mode is unstable (has an imaginary frequency) in all high-symmetry parent phases,
 391 which is unsurprising since these phases are not observed experimentally at low temperatures at any n for

392 the $\text{Ca}_{1+n}\text{Mn}_n\text{O}_{3n+1}$ series. The tilt stiffens between the parent and child phases for all n , showing that the
393 dynamic tilt couples competitively with the frozen in-plane rotation. In both the high- and low-symmetry
394 phases, the (imaginary) octahedral tilt frequency varies approximately linearly with Ca_2GeO_4 mole fraction,
395 although the stiffening effect going between the high- and low- symmetry phases becomes greater at higher
396 n (lower Ca_2GeO_4 fraction). The CaO rock salt layer also stiffens octahedral rotations and thus the angle
397 of the frozen rotation increases with n in rotation phases from 10.55° in $I4_1/acd$ Ca_2GeO_4 ($n = 1$) up to
398 the limit of 12.7° in $I4/mcm$ CaGeO_3 ($n = \infty$)(see Figure S2 in the SI). Hence, the greater amplitude
399 of frozen rotation observed in CaGeO_3 means that the competitive coupling between the frozen rotation
400 and dynamic tilt is greatest for this largest n member, and leads to further hardening of the dynamic tilt
401 frequency.

402 In the 0 GPa relaxed $\text{Ca}_{1+n}\text{Ge}_n\text{O}_{3n+1}$ structures, the tilt is still unstable for all n . However, it was found
403 previously (Ablitt et al. (2017)) that a discrepancy arises between the Ca_2GeO_4 and Ca_2MnO_4 in-plane
404 lattice parameters in the $I4_1/acd$ phase – due to in-plane magneto-strictive coupling – but that applying a
405 biaxial 4.3 GPa pressure corrects for this small difference, yielding very close agreement in the frequencies
406 of the softest phonon modes. After applying this biaxial pressure, the $n = 1$ $I4_1/acd$ Ca_2GeO_4 rotation
407 phase has all real mode frequencies, but the softest tilt in all structures with $n > 1$ is still unstable. This
408 agrees with experimental observation of the low temperature stable phases, shown as inset figures for each
409 composition on Figure 7.

410 $\text{Ca}_3\text{Mn}_2\text{O}_7$ is found at low temperature in the improper ferroelectric $A2_1am$ phase, but undergoes a
411 wide temperature region of phase coexistence with the uniaxial NTE $Acaa$ phase between 150-280 K on
412 cooling and 300-360 K on heating (Senn et al. (2015)). The strong first order nature of the phase transition
413 arises because frozen octahedral rotations in the $A2_1am$ and $Acaa$ phases have opposite sense (in-phase
414 vs out-of-phase about c within each perovskite layer – see Figure 8) but the approximate transformation
415 temperature gives an indication of the temperature at which octahedral tilts in a rotation phase develop
416 real frequencies. Furthermore, the $n = \infty$ perovskite, CaMnO_3 , transforms around 1166 K from a $Pnma$
417 ground state with frozen octahedral tilts, to an $I4/mcm$ phase with only an out-of-phase octahedral rotation
418 – the $n = \infty$ analogue of the $n = 2$ $Acaa$ – remaining in this phase for only a brief temperature window
419 before transforming again to the cubic parent structure at 1184 K (Taguchi et al. (1989)). For $n = 3$, the
420 reported symmetry for $\text{Ca}_4\text{Mn}_3\text{O}_{10}$ from 5 K up until room temperature is $Pbca$ (Battle et al. (1998)), in
421 which a static rotation and tilt of the octahedra are present, and, although to the best of our knowledge
422 a transformation to a higher-symmetry phase with only a frozen octahedral rotation has not yet been
423 reported², interpolating the experimental observations in Figure 7 predicts a transformation temperature
424 in the 250-1100 K window. The magnitude of the imaginary tilt frequency computed in Figure 7 may
425 therefore be interpreted as a crude indicator of the stability of the structure with condensed rotation and tilt
426 and thus of the temperature required to transform to the higher-symmetry rotation phase.

427 As well as having optimal elastic anisotropy to facilitate uniaxial NTE, the $n = 1$ Ca_2MnO_4 $I4_1/acd$
428 phase has soft tilt modes at low temperatures providing a thermodynamic driving force for cooperative
429 in-plane positive and out-of-plane negative thermal expansion. This feature is not unique to the $n = 1$
430 structure however, since at some higher temperature all $\text{Ca}_{1+n}\text{Mn}_n\text{O}_{3n+1}$ compounds should transform to a
431 phase in which the tilt frequencies are real and soft, at least over some temperature range. Furthermore, we
432 have demonstrated previously in the $\text{Ca}_{3-x}\text{Sr}_x\text{Mn}_2\text{O}_7$ system, that for a given layer thickness n , chemical
433 substitution (changing x) may be used to alter the Goldschmidt tolerance factor and thus the frequencies

² Although we do note that the high-symmetry $I4/mmm$ parent structure has been stabilised at room temperature from solid state synthesis at high temperatures and pressures (Yu et al. (2001)).

434 of these octahedral tilts, switching between positive and negative uniaxial thermal expansion (Senn et al.
435 (2016)). Therefore, Figure 7 shows that the Ruddlesden–Popper structure, through the layer thickness
436 n , determines a ballpark value for the 0 K tilt frequency in the uniaxial NTE phase, and thus a ballpark
437 temperature window in which the NTE phase will be stable. Hence, given this structural constraint we may
438 use chemical control to optimise the proximity of the structure to the phase transition and so enhance the
439 NTE. In this respect, the $n = 1$ family member, since one may presume that it may be tuned chemically to
440 arbitrary proximity to the competing phase transition, is the most promising candidate for exhibiting the
441 largest NTE on account of the anisotropy with respect to its most and least compliant directions which we
442 have shown is maximised for this system.

4 CONCLUSIONS

443 We have shown that the elastic anisotropy ratio, κ , found previously to be an essential ingredient for uniaxial
444 NTE, increases linearly in the Ruddlesden–Popper $\text{Ca}_{n+1}\text{Ge}_n\text{O}_{3n+1}$ series ($n = 1, 2, 3, 4 \dots \infty$) with the
445 $\text{CaGeO}_3\text{:CaO}$ content (expressed by the ratio $1/n$), reaching a maximum in the structure with maximal
446 interface ($n = 1$). By decomposing the components of the elastic compliance matrix for high-symmetry
447 and NTE phases (with a frozen octahedral rotation about the layering axis) into different regimes that show
448 similar trends with $1/n$, we have been able to link these regimes with internal degrees of freedom in the
449 structure that allow atomic mechanisms to operate that couple to cell strains. The most important of these
450 is the “corkscrew” mechanism that operates locally at the $\text{CaGeO}_3\text{:CaO}$ interface in phases with a frozen
451 octahedral rotation about the layering axis and therefore explains the trend that anisotropic compliance
452 correlates with the fraction of interface in these phases. This local atomic compliance mechanism is
453 analogous in certain ways to the wine-rack mechanism that operates in many much softer framework
454 materials. The compliance matrices can be rapidly calculated by DFT methods and diagonalised to
455 assess them for cross coupling terms that promote pronounced uni or biaxial NTE. This makes them
456 suitable descriptors for high throughput computational searching for novel NTE materials, especially when
457 symmetry constraints may be employed to narrow the space of candidate phases.

458 We further investigated the trend in frequency of octahedral tilts with RP layer thickness and found that
459 the 0 K tilt frequencies in NTE or analogous structures become softer with increasing n . This implies that a
460 window of stability of the NTE phase with soft active tilt modes exists at increasingly higher temperatures
461 with higher n . We had previously shown that the thermodynamic driver for NTE for a given n might
462 be tuned with chemical substitution, and we now show that the anisotropic compliance necessary for
463 NTE in these systems is maximised for a high fraction of $\text{CaGeO}_3\text{:CaO}$ interface layers in the structure.
464 On the basis of this analysis, we thus predict that the $n = 1$ systems, such as Ca_2MnO_4 , will be the
465 Ruddlesden–Popper systems in which the maximum NTE can be achieved via chemical substitution.

CONFLICT OF INTEREST STATEMENT

466 The authors declare that the research was conducted in the absence of any commercial or financial
467 relationships that could be construed as a potential conflict of interest.

AUTHOR CONTRIBUTIONS

468 CA performed all calculations and data analysis under the supervision of AM, NB and MS. All authors
469 contributed to the design of the study and partook in the discussion of the results. The paper was written by
470 CA and MS with contributions from NB and AM.

FUNDING

471 CA is supported by a studentship in the Centre for Doctoral Training on Theory and Simulation of Materials
472 at Imperial College London funded by the EPSRC (EP/ L015579/1). Calculations were performed on the
473 Imperial College London high-performance computing facility. This work was supported by the Thomas
474 Young Centre under grant TYC-101. We are grateful to the UK Materials and Molecular Modelling Hub
475 for computational resources, which is partially funded by EPSRC (EP/ P020194/1). MSS acknowledges
476 the Royal Society for a fellowship.

ACKNOWLEDGMENTS

477 The authors have no further acknowledgements in addition to those in the *Funding* Section.

SUPPLEMENTAL DATA

478 For supplementary material, see the attached file *SupplementaryMaterial.pdf*.

DATA AVAILABILITY STATEMENT

479 Data underlying this article can be accessed on figshare at DOI:10.6084/m9.figshare.6729287, and used
480 under the Creative Commons Attribution licence.

REFERENCES

- 481 (2012). The interface is still the device. *Nature Materials* 11, 91 EP –
- 482 Ablitt, C., Craddock, S., Senn, M. S., Mostofi, A. A., and Bristowe, N. C. (2017). The origin of uniaxial
483 negative thermal expansion in layered perovskites. *npj Computational Materials* 3, 44. doi:10.1038/
484 s41524-017-0040-0
- 485 Ablitt, C., Senn, M. S., Bristowe, N. C., and Mostofi, A. A. (in preparation). A corkscrew model for highly
486 coupled anisotropic compliance in ruddlesden–popper oxides with frozen octahedral rotations
- 487 Achary, S. N., Chakraborty, K. R., Patwe, S. J., Shinde, A. B., Krishna, P. S. R., and Tyagi, A. K. (2006).
488 Anisotropic thermal expansion behavior in tetragonal Sr₂MgWO₆. *Materials Research Bulletin* 41, 674
- 489 Ashcroft, N. W. and Mermin, N. D. (1976). *Solid State Physics* (Belmont, CA, USA: Brooks/Cole)
- 490 Azuma, M., Chen, W. T., Seki, H., Czapski, M., Olga, S., Olga, K., et al. (2011). Colossal negative thermal
491 expansion in BiNiO_3 induced by intermetallic charge transfer. *Nat. Commun.* 2, 347
- 492 Barron, T. H. K. and Munn, R. W. (1967). Analysis of the thermal expansion of anisotropic solids:
493 Application to zinc. *Philosophical Magazine* 15, 85
- 494 Battle, P. D., Green, M. A., Lago, J., Millburn, J. E., Rosseinsky, M. J., and Vente, J. F. (1998). Crystal and
495 magnetic structures of $\text{Ca}_4\text{Mn}_3\text{O}_{10}$, an $n = 3$ ruddlesden–popper compound. *Chemistry of Materials* 10,
496 658–664. doi:10.1021/cm970647r
- 497 Benedek, N. A. and Fennie, C. J. (2011). Hybrid improper ferroelectricity: A mechanism for controllable
498 polarization–magnetization coupling. *Phys. Rev. Lett.* 106, 107204
- 499 Benedek, N. A., Rondinelli, J. M., Djani, H., Ghosez, P., and Lightfoot, P. (2015). Understanding
500 ferroelectricity in layered perovskites: new ideas and insights from theory and experiments. *Dalton*
501 *Trans.* 44, 10543–10558. doi:10.1039/C5DT00010F
- 502 Borzi, R. A., Grigera, S. A., Farrell, J., Perry, R. S., Lister, S. J. S., Lee, S. L., et al. (2007). Formation of a
503 nematic fluid at high fields in $\text{Sr}_3\text{Ru}_2\text{O}_7$. *Science* 315, 214–217. doi:10.1126/science.1134796

- 504 Chen, J., Wang, F., Huang, Q., Hu, L., Song, X., Deng, J., et al. (2013). Effectively control negative thermal
505 expansion of single-phase ferroelectrics of $\text{pbtio}_3\text{-(bi,la)feo}_3$ over a giant range. *Sci. Rep.* 3, 2458
- 506 Clark, S. J., Segall, M. D., Pickard, C. J., Hasnip, P. J., Probert, M. J., Refson, K., et al. (2005). First
507 principles methods using castep. *Z. Kristall.* 220, 567–570
- 508 Cordrey, K. J., Stanczk, M., Dixon, C. A. L., Knight, K. S., Gardner, J., Morrison, F. D., et al. (2015).
509 Structural and dielectric studies of the phase behaviour of the topological ferroelectric $\text{La}_{1-x}\text{Nd}_x\text{TaO}_4$.
510 *Dalton Trans.* 44
- 511 Dove, M. T. (1993). *Introduction to Lattice Dynamics* (Cambridge University Press)
- 512 Dove, M. T., Heine, V., and Hammond, K. D. (1995). Rigid unit modes in framework silicates. *Min. Mag.*
513 59, 629–639
- 514 Dwivedi, A. and Cormack, A. N. (1991). Crystal chemistry of ruddlesden-popper type structures in high T_c
515 ceramic superconductors. *Bulletin of Materials Science* 14, 575–584. doi:10.1007/BF02744688
- 516 Fortes, A. D., Suard, E., and Knight, K. S. (2011). Negative linear compressibility and massive anisotropic
517 thermal expansion in methanol monohydrate. *Science* 331, 742–746. doi:10.1126/science.1198640
- 518 Glasser, L. (2017). Systematic thermodynamics of layered perovskites: Ruddlesden–popper phases.
519 *Inorganic Chemistry* 56, 8920–8925. doi:10.1021/acs.inorgchem.7b00884. PMID: 28737898
- 520 Grima, J. N., Caruana-Gauci, R., Attard, D., and Gatt, R. (2012). Three-dimensional cellular structures
521 with negative poisson's ratio and negative compressibility properties. *Proceedings of the Royal Society*
522 *of London A: Mathematical, Physical and Engineering Sciences* doi:10.1098/rspa.2011.0667
- 523 Grima, J. N. and Evans, K. E. (2000). Auxetic behavior from rotating squares. *Journal of Materials*
524 *Science Letters* 19, 1563–1565. doi:10.1023/A:1006781224002
- 525 Grüneisen, E. and Goens, E. (1924). Thermal expansion of zinc and cadmium. *Z. Phys.* 29, 141
- 526 Haeni, J. H., Theis, C. D., Schlom, D. G., Tian, W., Pan, X. Q., Chang, H., et al. (2001). Epitaxial growth
527 of the first five members of the $\text{sr}_{n+1}\text{tino}_3\text{n}+1$ ruddlesden-popper homologous series. *Applied Physics*
528 *Letters* 78, 3292–3294. doi:10.1063/1.1371788
- 529 Hatt, A. J. and Spaldin, N. A. (2010). Structural phases of strained laalo_3 driven by octahedral tilt
530 instabilities. *Phys. Rev. B* 82, 195402. doi:10.1103/PhysRevB.82.195402
- 531 Heine, V., Welche, P. R. L., and Dove, M. T. (1999). Geometrical origin and theory of negative thermal
532 expansion in framework structures. *Journal of the American Ceramic Society* 82, 1793–1802. doi:10.
533 1111/j.1151-2916.1999.tb02001.x
- 534 Huang, L.-F., Lu, X.-Z., and Rondinelli, J. M. (2016). Tunable negative thermal expansion in layered
535 perovskites from quasi-two-dimensional vibrations. *Phys. Rev. Lett.* 117, 115901
- 536 Lee, C.-H., Podraza, N. J., Zhu, Y., Berger, R. F., Shen, S., Sestak, M., et al. (2013). Effect of
537 reduced dimensionality on the optical band gap of srtio_3 . *Applied Physics Letters* 102, 122901.
538 doi:10.1063/1.4798241
- 539 Mackenzie, A. P. and Maeno, Y. (2003). The superconductivity of sr_2ruo_4 and the physics of spin-triplet
540 pairing. *Rev. Mod. Phys.* 75, 657–712. doi:10.1103/RevModPhys.75.657
- 541 McCoy, M. A., Grimes, R. W., and Lee, W. E. (1997). Phase stability and interfacial structures in the
542 sro-srtio_3 system. *Philosophical Magazine A* 75, 833–846. doi:10.1080/01418619708207205
- 543 Palgrave, R. G., Borisov, P., Dyer, M. S., McMitchell, S. R. C., Darling, G. R., Claridge, J. B., et al. (2012).
544 Artificial construction of the layered ruddlesden-popper manganite $\text{la}_2\text{sr}_2\text{mn}_3\text{o}_{10}$ by reflection high
545 energy electron diffraction monitored pulsed laser deposition. *Journal of the American Chemical Society*
546 134, 7700–7714. doi:10.1021/ja211138x. PMID: 22463768

- 547 Perdew, J. P., Ruzsinszky, A., Csonka, G. I., Vydrov, O. A., Scuseria, G. E., Constantin, L. A., et al. (2008).
548 Restoring the density-gradient expansion for exchange in solids and surfaces. *Phys. Rev. Lett.* 100,
549 136406
- 550 Qi, T. F., Korneta, O. B., Parkin, S., De Long, L. E., Schlottmann, P., and Cao, G. (2010). Negative volume
551 thermal expansion via orbital and magnetic orders in $\text{Ca}_2\text{Ru}_{1-x}\text{Cr}_x\text{O}_4$ ($0 < x < 0.13$). *Phys. Rev. Lett.*
552 105, 177203. doi:10.1103/PhysRevLett.105.177203
- 553 Refson, K., Tulip, P. R., and Clark, S. J. (2006). Variational density-functional perturbation theory for
554 dielectrics and lattice dynamics. *Phys. Rev. B* 73, 155114
- 555 Sarlosi, J. and Bocko, J. (2016). Effective material moduli for composites. *American Journal of Mechanical*
556 *Engineering* 4, 289–292. doi:10.12691/ajme-4-7-11
- 557 Senn, M. S., Bombardi, A., Murray, C. A., Vecchini, C., Scherillo, A., Lui, X., et al. (2015). Negative
558 thermal expansion in hybrid improper ferroelectric ruddlesden-popper perovskites by symmetry trapping.
559 *Phys. Rev. Lett.* 114, 035701. doi:10.1103/PhysRevLett.114.035701
- 560 Senn, M. S., Murray, C. A., Luo, X., Wang, L., Huang, F.-T., Cheong, S.-W., et al. (2016). Symmetry
561 switching of negative thermal expansion by chemical control. *J. Am. Chem. Soc.* 138, 5479. doi:10.
562 1021/jacs.5b13192
- 563 Shannon, R. D. (1976). Revised effective ionic radii and systematic studies of interatomic distances in
564 halides and chalcogenides. *Acta Crystallographica*, 751–767
- 565 Smith, C., Grima, J., and Evans, K. (2000). A novel mechanism for generating auxetic behaviour in
566 reticulated foams: missing rib foam model. *Acta Materialia* 48, 4349 – 4356. doi:https://doi.org/10.
567 1016/S1359-6454(00)00269-X
- 568 Taguchi, H., Nagao, M., Sato, T., and Shimada, M. (1989). High-temperature phase transition of CaMnO_3 - δ .
569 *Journal of Solid State Chemistry* 78, 312 – 315. doi:https://doi.org/10.1016/0022-4596(89)90113-8
- 570 Takahashi, J. and Kamegashira, N. (1993). X-ray structural study of calcium manganese oxide by rietveld
571 analysis at high temperatures. *MRS Bulletin* 28, 565 – 573
- 572 Wang, L., Luo, H., Deng, S., Sun, Y., and Wang, C. (2017). Uniaxial negative thermal expansion,
573 negative linear compressibility, and negative poisson's ratio induced by specific topology in $\text{Zn}[\text{Au}(\text{CN})_2]_2$.
574 *Inorganic Chemistry* 56, 15101–15109. doi:10.1021/acs.inorgchem.7b02416. PMID: 29189011
- 575 Weber, M. C., Guennou, M., Dix, N., Pesquera, D., Sánchez, F., Herranz, G., et al. (2016). Multiple
576 strain-induced phase transitions in LaNiO_3 thin films. *Phys. Rev. B* 94, 014118. doi:10.1103/PhysRevB.
577 94.014118
- 578 Yan, L., Niu, H. J., Duong, G. V., Suchomel, M. R., Bacsá, J., Chalker, P. R., et al. (2011). Cation ordering
579 within the perovskite block of a six-layer ruddlesden-popper oxide from layer-by-layer growth - artificial
580 interfaces in complex unit cells. *Chem. Sci.* 2, 261–272. doi:10.1039/C0SC00482K
- 581 Yoshida, Y., Ikeda, S.-I., Matsuhata, H., Shirakawa, N., Lee, C. H., and Katano, S. (2005). Crystal and
582 magnetic structure of $\text{Ca}_3\text{Ru}_2\text{O}_7$. *Phys. Rev. B* 72, 054412. doi:10.1103/PhysRevB.72.054412
- 583 Yoshizawa, H., Kakeshita, T., Kajimoto, R., Tanabe, T., Katsufuji, T., and Tokura, Y. (2000). Stripe
584 order at low temperatures in $\text{La}_{2-x}\text{Sr}_x\text{NiO}_4$ with $0.289 \lesssim x \lesssim 0.5$. *Phys. Rev. B* 61, R854–R857.
585 doi:10.1103/PhysRevB.61.R854
- 586 Yu, R. C., Li, S. Y., Zhu, J. L., Li, F. Y., Zhang, Z., Jin, C. Q., et al. (2001). Ideal $n=3$ phase $\text{Ca}_4\text{Mn}_3\text{O}_{10}$
587 of ruddlesden–popper series obtained using high pressure and high temperature. *Journal of Applied*
588 *Physics* 90, 6302–6306. doi:10.1063/1.1419205

1 BACKGROUND THEORY

589 This section briefly summarises some of the background theory relevant for understanding thermal
 590 expansion in an anisotropic material. An interested reader can find many more thorough explanations of
 591 these concepts in other sources (Ashcroft and Mermin (1976), Dove (1993)).

592 The elastic compliance matrix, \mathbf{s} , relates the anisotropic strain response of a material, $\boldsymbol{\varepsilon}$ to an applied
 593 stress, $\boldsymbol{\sigma}$, via the equation

$$\varepsilon_i = \sum_j s_{ij} \sigma_j, \quad (7)$$

594 where ε_i (σ_i) is component i of $\boldsymbol{\varepsilon}$ ($\boldsymbol{\sigma}$) and $\boldsymbol{\varepsilon}$ ($\boldsymbol{\sigma}$) is a 6-dimensional vector expressed in Voigt notation so
 595 that the first three components ($i = 1, 2, 3$) describe normal strains (stresses) of the crystal and the latter
 596 three components ($i = 4, 5, 6$) describe shear strains (stresses). \mathbf{s} is therefore a 6×6 matrix.

597 Using this definition of \mathbf{s} , the general anisotropic thermal expansion, $\boldsymbol{\alpha}$, of a material is given by the
 598 equation

$$\boldsymbol{\alpha} = \mathbf{s} \boldsymbol{\Phi}, \quad (8)$$

599 where $\boldsymbol{\alpha}$ is the anisotropic thermal expansion vector expressed in Voigt notation, in response to an
 600 anisotropic driving force for thermal expansion, that we express by the vector $\boldsymbol{\Phi}$.

601 In a tetragonal material, the a and b axes are equivalent, and thus in the compliance matrix $s_{11} = s_{22}$ and
 602 $s_{13} = s_{23}$. Furthermore, all normal-shear coupling terms, s_{ij} ($i = 1, 2, 3; j = 4, 5, 6$), are 0 by symmetry
 603 and thus shear components of $\boldsymbol{\Phi}$ may not contribute to normal components of $\boldsymbol{\alpha}$. If we assume that we
 604 have a tetragonal material that remains tetragonal, and thus undergoes no shear deformations, Equation 8
 605 simplifies to:

$$\begin{pmatrix} \alpha_1(T) \\ \alpha_2(T) \\ \alpha_3(T) \end{pmatrix} = \begin{pmatrix} s_{11} & s_{12} & s_{13} \\ s_{12} & s_{22} & s_{13} \\ s_{13} & s_{13} & s_{33} \end{pmatrix} \begin{pmatrix} \Phi_1(T) \\ \Phi_2(T) \\ \Phi_3(T) \end{pmatrix}. \quad (9)$$

606 In Equation 9 we assume that \mathbf{s} is temperature independent to a first approximation and therefore
 607 the temperature dependence of $\boldsymbol{\alpha}$ is given by the driving force for thermal expansion $\boldsymbol{\Phi}(T)$. We may
 608 then express $\boldsymbol{\Phi}(T)$ in terms of mode specific heat capacities, $C_v^i(T)$, and anisotropic mode Grüneisen
 609 parameters, γ^i , by the equation

$$\Phi_\eta(T) = \sum_i C_v^i(T) \gamma_\eta^i. \quad (10)$$

610 In Equation 10 the summation over indices i is really of every discrete phonon mode at every phonon
 611 wavevector on a sufficiently dense grid to approximate an integral over the Brillouin zone. The specific
 612 heat capacity of mode i is a function of the frequency of that mode, ω^i , and temperature T ,

$$C_v^i = \frac{\hbar w^i}{V} \frac{\partial}{\partial T} \left[\left(e^{\frac{\hbar w^i}{k_B T}} - 1 \right)^{-1} \right], \quad (11)$$

613 where the derivative describes how the population of that mode increases with increasing T . The
 614 component γ_η^i of the vector γ^i then describes the contribution of mode i to thermal expansion of lattice
 615 parameter η , and is defined as

$$\gamma_\eta^i = -\frac{\partial \ln [w^i]}{\partial \ln [\eta]}, \quad (12)$$

616 such that if $\gamma_\eta^i > 0$ mode i contributes to PTE of η and likewise if $\gamma_\eta^i < 0$ mode i contributes to NTE.

617 Equation 9 implies that even a Φ vector with all positive components could be transformed into a uniaxial
 618 or biaxial NTE regime (α with one or two negative components respectively) by a sufficiently anisotropic
 619 compliance matrix. This scenario is illustrated for a tetragonal material in Figure 2 where a Φ driving bulk
 620 PTE is transformed by a highly anisotropic s into the quadrant corresponding to uniaxial NTE of the c axis.

621 The degree of anisotropy can be quantified by the ratio, κ , of the highest and lowest eigenvalues of s , s_H
 622 and s_L respectively, given as

$$\kappa = \frac{s_H}{s_L}. \quad (13)$$

623 If $\kappa = 1$, the quadratic form of s in Figure 2 would be a sphere and s would not alter the direction of the
 624 vector Φ in Equation 8. However, as κ becomes greater, the quadratic form of s becomes more ellipsoidal
 625 and thus s has the potential to rotate the direction of Φ . κ is thus a good metric to consider the potential for
 626 s to transform Φ driving bulk PTE into α corresponding to anisotropic NTE.

2 PHASE DIAGRAM AND SYMMETRY OF RUDDLESDEN–POPPER PHASES

627 In Figure 1, members of the $A_{n+1}B_nO_{3n+1}$ Ruddlesden–Popper series were displayed in the high-symmetry
 628 $I4/mmm$ parent structure. Figure 8 shows the phase diagrams relevant for NTE in the $n = 1$ and $n = 2$
 629 systems. In Ca_2MnO_4 and $\text{Ca}_3\text{Mn}_2\text{O}_7$, the uniaxial NTE phase has an anti-phase frozen octahedral rotation
 630 about the c axis, corresponding to the $I4_1/acd$ or $Acaa$ space groups respectively. In $n = 1$ $I4_1/acd$,
 631 this rotation is anti-phase between adjacent equivalent BO_6 perovskite layers in different unit cells – the
 632 corresponding distortion is at $P = (1/2, 1/2, 1/2)$ – whereas in $n = 2$ $Acaa$ the rotations are anti-phase within
 633 each BO_6 block but with no doubling of the $I4/mmm$ unit cell along c – corresponding to a distortion at
 634 $X = (1/2, 1/2, 0)$. In both systems, this NTE phase with anti-phase rotations competes with a *ground-state*
 635 phase with both frozen rotations (about c) and tilts (with rotation axes in the layering plane) of BO_6
 636 octahedra, that is a child of an alternative rotation phase with in-phase rotations. The *ground-state* phase
 637 shown is found to be the lowest energy structure computed using DFT in $\text{Ca}_{n+1}\text{Ge}_n\text{O}_{3n+1}$. The analogous
 638 phase diagram for an ABO_3 perovskite (the $n = \infty$ RP end-member) is also shown for comparison, even
 639 though ABO_3 perovskites typically do not exhibit uniaxial NTE in their $I4/mcm$ phase with anti-phase
 640 rotations.

641 We previously used the concept of *symmetry trapping* to explain the presence of soft (low frequency), yet
 642 stable (real phonon frequencies), octahedral tilts driving uniaxial NTE in $n = 2$ $\text{Ca}_3\text{Mn}_2\text{O}_7$ (Senn et al.

643 (2015)). This idea stems from the fact in the $n = 1, 2$ phase diagrams, that the crystal cannot transform from
 644 the NTE metastable phase to the ground-state phase without the frozen octahedral rotations changing sense
 645 – anti-phase rotations about c need to “unwind” to form the in-phase rotations in the ground-state phase.
 646 Thus soft phonons are able to persist without the structure undergoing a soft-mode phase transition to the
 647 ground state. In the ABO_3 perovskite, the c axis is not as strongly defined as in layered RP compounds
 648 (since there is no inherent layering topologically distinguishing a particular axis in the ABO_3 structure).
 649 Therefore, although there is no group-subgroup relationship between $I4/mcm$ and the ground-state $Pnma$
 650 phases, there is no clear distinction between rotations and tilts and a phase transition with a relatively low
 651 activation barrier corresponding to a rotation of the direction of the out-of-phase octahedral tilting can be
 652 envisaged.

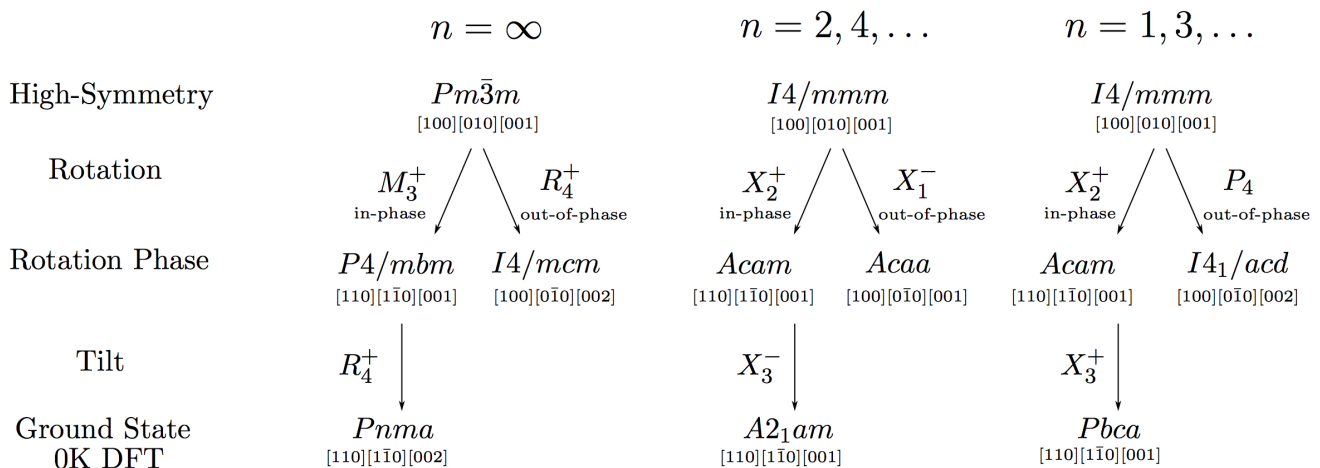


Figure 8. Space-group diagrams showing the relevant phases for uniaxial NTE in low n $A_{n+1}B_nO_{3n+1}$ Ruddlesden–Popper systems. The NTE phase has a frozen rotation of BO_6 octahedra about the layering axis, which is out-of-phase between adjacent unit cells (P_4 irrep) if $n = 1$ and out-of-phase with each perovskite block but in-phase between adjacent unit cells (X_1^- irrep) in the $n = 2$ system. This NTE phase competes with a ground state phase that has an in-phase frozen octahedral rotation about the layering axis and frozen octahedral tilt in the plane of the layering axis. For higher n , the $n = 1$ picture extends to odd values of n and the $n = 2$ to even values of n . An analogous phase diagram for the $n = \infty$ extreme of an ABO_3 perovskite is also shown even though the $I4/mcm$ phase seldom exhibits NTE.

653 The $n = 1$ phase diagram may be extended to all odd n in the Ruddlesden–Popper series and the $n = 2$
 654 phase diagram to all even n . In this work, we distinguish between high-symmetry phases – the $I4/mmm$
 655 RP or $Pm\bar{3}m$ perovskite parents – and rotation phases – by which we mean the NTE (or equivalent) phase
 656 with anti-phase rotations about the c axis – in first-principles simulations of the $Ca_{n+1}Ge_nO_{3n+1}$ system
 657 ($n = 1, 2, 3, 4, \infty$).

658 Although the $Acam$ and $Acaa$ rotation phases have orthorhombic space groups, in DFT simulations in
 659 this work and from experimental measurement in previous works (Senn 2015) we in fact find them to
 660 be pseudo-tetragonal. This is because locally each BO_6 octahedron has 4-fold rotational symmetry and
 661 the frozen rotation angle is the same for octahedra in equivalent layer positions in different perovskite
 662 blocks in the unit cell, even if the sense (clockwise vs anticlockwise) of the rotation is different. This
 663 pseudo-tetragonality means that even though structures were relaxed in orthorhombic space groups with no
 664 additional symmetry constraints, the a and b lattice parameters are always found to be equal to within the
 665 accuracy of the simulation with no spontaneous in-plane distortion of the BO_6 units.

666 In the $n = 1, 3$ compounds, the structures (lattice parameters, relaxed cell energies, octahedral rotation
667 angles) of the $Acam$ and $I4_1/acd$ phases were exactly equal (to the accuracy of the calculation), indicating
668 that equivalent GeO_6 octahedra in adjacent $I4_1/mmm$ unit cells are sufficiently de-phased that the relative
669 sense of their rotations has no effect on the structural properties of the crystal. Noting that in $n = 3$
670 $Acam$ the octahedral rotations are anti-phase within each perovskite block, exactly as in relaxed $I4_1/acd$
671 (although still in-phase between unit cells), we used $n = 3 Acam$ as a proxy for $I4_1/acd$ in calculations
672 of elastic properties in Sections 3.2-3.1 since many repeated cell relaxations were required that would
673 have been extremely computationally expensive in the large $n = 3 I4_1/acd$ unit cell. However, for lattice
674 dynamics calculations, $n = 3 I4_1/acd$ was studied since the phase of rotations between unit cells was
675 found to give different frequencies for the softest tilt modes between $Acam$ and $I4_1/acd$ in the lattice
676 dynamical calculations performed in Section 3.4.